

A Two-step-training Deep Learning Framework for Real-time Computational Imaging without Physics Priors

RUIBO SHANG, KEVIN HOFFER-HAWLIK, AND GEOFFREY P. LUKE*

Thayer School of Engineering, Dartmouth College, 14 Engineering Dr., Hanover, NH 03755, USA

**geoffrey.p.luke@dartmouth.edu*

ABSTRACT

Deep learning (DL) is a powerful tool in computational imaging for many applications. A common strategy is to reconstruct a preliminary image as the input of a neural network to achieve an optimized image. Usually, the preliminary image is acquired with the prior knowledge of the imaging model. One outstanding challenge, however, is that the model is sometimes difficult to acquire with high accuracy or it can be nonlinear. Another main challenge is that computational imaging algorithms for the preliminary image reconstruction are time consuming and cannot achieve real-time imaging. In this work, a two-step-training DL (TST-DL) framework is proposed for real-time computational imaging without prior knowledge of the model. A single fully-connected layer (FCL) is trained to directly learn the model with the raw measurement data as input and the image as output. Then, this pre-trained FCL is fixed and concatenated with an untrained deep convolutional network (U-Net) for a second-step training to improve the output image fidelity. This approach has four main advantages. First, no prior knowledge of the model is required since the first-step training is to directly learn the model. Second, real-time imaging can be achieved since the raw measurement data is directly used as the input to the model. Third, it can handle any size and dimensionality of the network input and solve the input-output size-and dimensionality- mismatch issues which arise in convolutional neural networks. Fourth, it can overcome the overburdening issue in the established end-to-end DL approaches by learning the model and the optimal regularizer individually. We demonstrate this framework in the applications of single-pixel imaging and photoacoustic imaging for linear model cases. The results are quantitatively compared with those from other DL frameworks and model-based iterative optimization approaches. Noise robustness and the required size of the training dataset are studied for this framework. We further extend this concept to nonlinear models in the application of image de-autocorrelation by using multiple FCLs in the first-step training. Overall, this TST-DL framework is widely applicable to virtually any computational imaging modalities for real-time image reconstruction without physics priors.

INTRODUCTION

Computational Imaging is a powerful tool in the applications of image reconstruction. It relaxes the hardware requirements of imaging systems by relying on (typically iterative) computational techniques to recover the lost information, that is, solving an inverse imaging problem computationally^{1, 2}. These methods rely on a measured or assumed forward operator of the imaging system to create a mapping from the image to the measurement. However, the forward operator is often ill-posed by design or due to the imperfect physical measurement, meaning multiple solutions exist for a given measurement. Therefore, additional information about the scene or the object must be incorporated in the computational process for accurate reconstruction.

One of the most common methods in computational imaging is sparsity-based optimization which seeks to reconstruct images from incomplete data or an ill-posed forward operator^{3, 4}. This concept is based on the knowledge that most natural images are sparse (i.e., only a few nonzero values exist) when transformed into a specific domain. Researchers have successfully applied sparsity-based optimization in a variety of imaging fields ranging from compressed ultrafast photography⁵ to holographic video⁶ to biomedical imaging⁷. Although sparsity-based optimization has advantages in image reconstruction, the primary drawback to this approach is that it is iterative and time consuming. Depending on the scale and scope of the problem, an image reconstruction task can require minutes to even hours of computation. Therefore, it cannot achieve real-time imaging for many applications which require pipelined data acquisition and image reconstruction. Furthermore, the optimal algorithm-specific parameters in the sparsity-based optimization must be heuristically determined.

Deep learning (DL)^{2, 8} is an emerging computational imaging approach dramatically improving the state-of-the-art in fast image reconstruction^{9, 10, 11, 12, 13, 14}. Instead of building a specific model and finding the optimal algorithm-specific parameters heuristically (as in sparsity-based optimization approaches), it relies on large amounts of data to automatically learn tasks by using the backpropagation algorithm to find the optimal parameters in each layer of a neural network⁸. It has the benefit of being computationally efficient since most of the computational energy is used during the one-time training process. Compared with sparsity-based optimization approaches which require iterative testing of the regularizer for each image¹⁵, DL approaches utilize the training dataset to find the optimal regularizer for the broad range of images. Therefore, DL is a promising alternative to augment or replace the iterative algorithms used in sparsity-based optimization. Researchers have applied the DL approach in many imaging fields with varying network structures². The U-Net¹⁶ architecture is one of the most successful DL frameworks in the imaging field. Its architecture consists of a contracting path to capture context and a symmetric expanding path for precise localization. Skip connections between the contracting and expanding path help to preserve features from the input image. A variety of applications in the imaging field have harnessed the original or a modification of the U-Net structure ranging from segmentation to image reconstruction from incomplete data^{17, 18, 19, 20, 21, 22, 23}. Despite the advantages of these DL approaches in computational imaging, there are still some limitations. First, a large dataset is usually required to train the network and it must span the space of possible images one would expect to encounter. Second, most of the current DL techniques still require knowledge of the imaging forward model for an initial image guess to feed into the DL networks^{14, 21, 24, 25}. However, the forward model in many imaging fields can be difficult to acquire with high accuracy^{7, 26, 27, 28} or it can be nonlinear^{14, 29}. Furthermore, the reconstruction of the initial image guess will sometimes be computationally intensive, especially when using the iterative reconstruction approaches^{30, 31}. Third, most of the DL approaches are designed for a specific application and not widely applicable in other problems. For instance, mismatches of the size and dimensionality between the measurement data and the reconstructed image are not easily addressed in the U-Net architecture which usually requires the input and output images to have the same size and dimensionality¹⁶. Although a modified U-Net framework in²² can deal with the image size mismatch issues, it still requires a two-dimensional (2D) image as the input.

In this paper, a two-step-training DL (TST-DL) framework is proposed for real-time DL-based computational image reconstruction without prior knowledge of the forward model. The first step trains a single fully-connected layer (FCL) (for linear imaging models) or multiple FCLs (for nonlinear imaging models) to approximate the imaging inverse model with the raw measurement data as input and the ground-truth image as output. The weights of this trained FCL are then fixed and concatenated with an untrained convolutional neural network (U-Net) for a second-step training to effectively

impose regularization constraints and improve the reconstruction quality of the results predicted from the first-step training. This versatile DL approach is beneficial because it can be applied to virtually any computational imaging system without the prior knowledge of the imaging model (directly learning the model instead) and overcome the overburdening issues (learning the model and the optimal regularizer simultaneously) in the established end-to-end DL approaches. Furthermore, it can yield results in real time with comparable performance to the iterative algorithms. Moreover, it can handle any size or dimensionality of the network input and solve the input-output image size- and dimensionality- mismatch issues. Finally, by incorporating minor changes to the TST-DL network, image reconstruction with nonlinear imaging models can be performed.

RESULTS

Our TST-DL framework follows an FCL (or multiple FCLs for nonlinear models) and a U-Net architecture as shown in Fig. 1. The DL framework in step 1 consists of an FCL mapping from the raw measurement data (input) to the image (output) (Batch-normalization (BatchNorm), reshape and permute layers are used for normalization and reshape purposes). With this FCL, the input measurement data and the output image do not need to have the same size or even the same dimensionality. By training the FCL, the optimal inverse operator will be learned given the training datasets. The DL framework in step 2 follows the U-Net architecture concatenated with the pre-trained FCL from step 1. The U-Net, which utilizes an encoder-decoder structure with skip connections to preserve wide-frequency features, was chosen because of its success in solving image-to-image problems. This TST-DL is inspired by the regularized optimization as demonstrated in **Methods**.

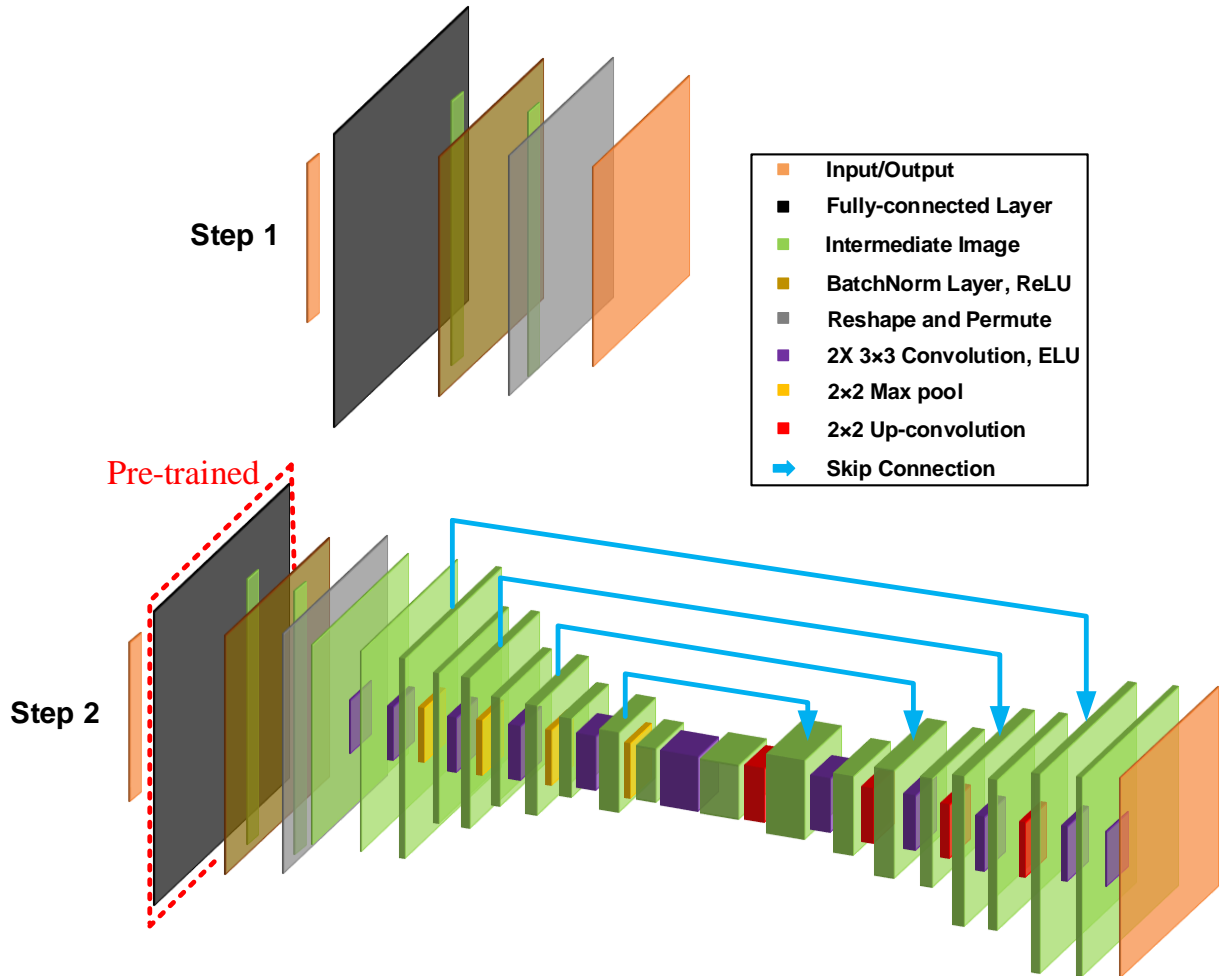


Fig. 1. TST-DL structure. Step 1 is training the FCL and step 2 is training a U-Net concatenated with the fixed pre-trained FCL. The input is the raw measurement data that can be any size and dimension and the output is a 2D image.

The data acquisition and results from the prediction of the TST-DL for the single-pixel imaging with Russian-Doll (RD) Hadamard³² and random Hadamard patterns, photoacoustic (PA) imaging^{33, 34, 35}, and image de-autocorrelation

are shown in this section with the simulated data. Two experiments (single-pixel imaging with random grayscale patterns and PA imaging) were conducted as the experimental verification of TST-DL's effectiveness. Quantitative comparisons are made with other DL frameworks (a deep convolutional auto-encoder network (DCAN)³⁶, one-step-training DL (OST-DL) and U-Net) and the established model-based optimization approaches (an iterative L_2 norm minimization approach LSQR³⁰ and a two-step iterative shrinkage/thresholding (TwIST) algorithm³¹). Note that the U-Net approach assumes accurate initial guess of the image with the knowledge of the model while the LSQR and TwIST methods require precise knowledge of the forward model. The usage of DCAN, U-Net and OST-DL are detailed in **Methods**.

Single-pixel imaging with RD Hadamard patterns

In the first case, the RD Hadamard patterns are used in the single-pixel imaging. In RD Hadamard patterns, the measurement order of the Hadamard basis is reordered and optimized according to their significance for general scenes, such that at discretized increments, the complete sampling for different spatial frequencies is obtained³². The STL-10 natural image database³⁷ was used as the image database for training all the DL networks with 6 compression ratios. The details of the training procedures are demonstrated in **Methods**.

The reconstructed images at 4X and 8X compression ratios from multiple reconstruction approaches are shown in Fig. 2. The images from the TST-DL are shown in the last column and compared with the other three DL frameworks (DCAN, OST-DL and U-Net) and the established model-based optimization approaches (LSQR and TwIST). The intermediate results from the first-step training using the FCL in TST-DL are also shown as FCL-DL. Supplementary Table 1 shows the averaged root mean squared error (RMSE) and structural similarity index (SSIM)³⁸ of the reconstructed images in the testing dataset at 4X and 8X compression ratios from all the reconstruction approaches (For TwIST, 500 images in the testing dataset were reconstructed and used to calculate the averaged RMSE and SSIM instead of the full testing dataset in the interest of time). From Fig. 2 and Supplementary Table 1, we can see that the results from DL approaches are comparable to those from the established model-based optimization approaches (LSQR and TwIST). Importantly, both LSQR and TwIST approaches require accurate knowledge of the forward model for image optimization. In addition, reconstruction from LSQR and TwIST require thousands of iterations, which cannot achieve real-time imaging. Therefore, for real-time imaging with the forward model acquired in low accuracy or even not available, LSQR and TwIST are not the best options.

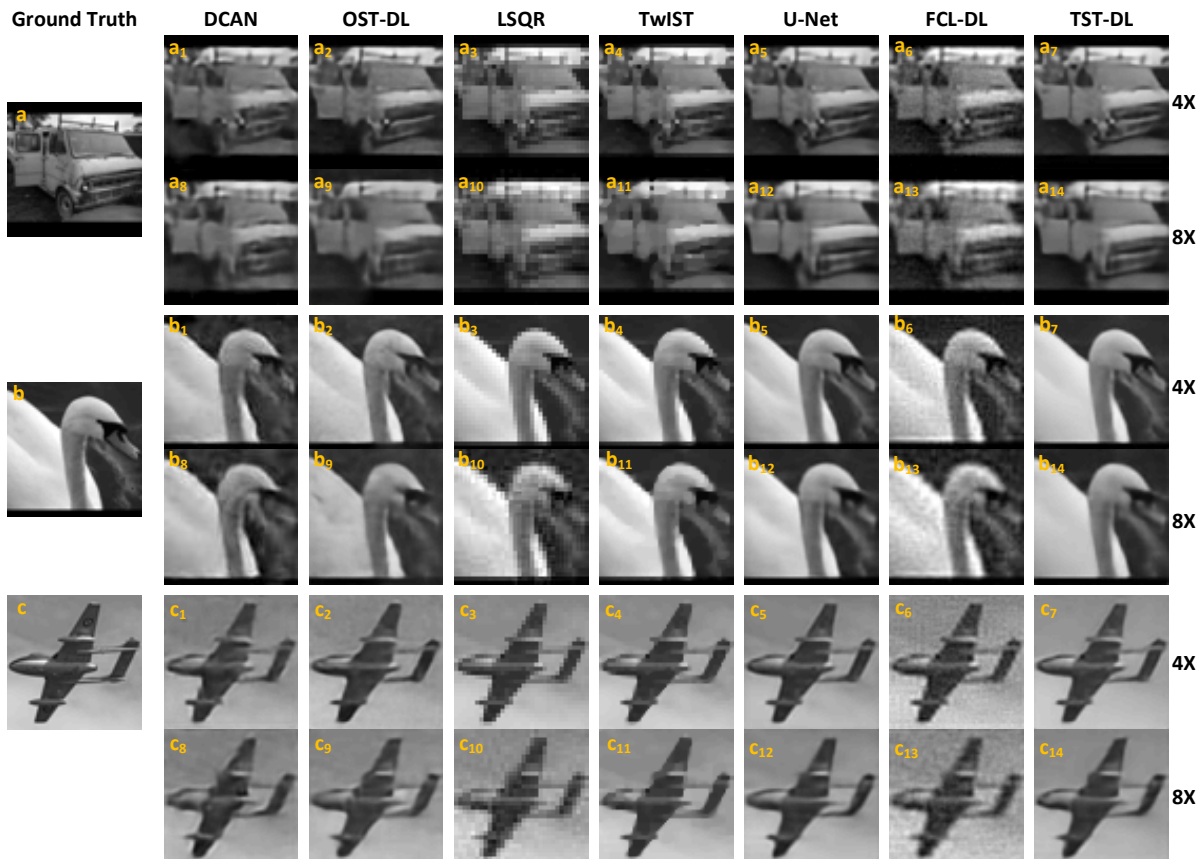


Fig. 2. Three representative reconstructed images in the testing dataset from DCAN, OST-DL, LSQR, TwIST, U-Net, FCL-DL and TST-DL at 4X and 8X compression ratios and their ground-truth images. (a) The ground-truth image of a van. (a₁-a₇) The reconstructed van images from all the approaches respectively at the 4X compression ratio. (a₈-a₁₄) The reconstructed van images from all the approaches respectively at the 8X compression ratio. (b) The ground-truth image of a swan. (b₁-b₇) The reconstructed swan images from all the approaches respectively at the 4X compression ratio. (b₈-b₁₄) The reconstructed swan images from all the approaches respectively at the 8X compression ratio. (c) The ground-truth image of an aircraft. (c₁-c₇) The reconstructed aircraft images from all the approaches respectively at the 4X compression ratio. (c₈-c₁₄) The reconstructed aircraft images from all the approaches respectively at the 8X compression ratio.

For further quantitative comparison with the other three DL frameworks, the mean and the standard deviation of the RMSE and SSIM are calculated through the 2,000 testing images at all the compression ratios as shown in Fig. 3. We can see that for most of the cases, the U-Net approach is the best. This makes sense since the initial guess of the input images in U-Net needs the physics priors of the model. It is obvious that the reconstruction results will be better when the exact model is incorporated in the framework. For TST-DL, even though the physics priors of the model are unknown, the results are almost equivalent to those from U-Net and outperform those from DCAN and OST-DL. Therefore, for approaches without the physics priors of the model, TST-DL is the best in terms of RMSE and SSIM for all compression ratios.

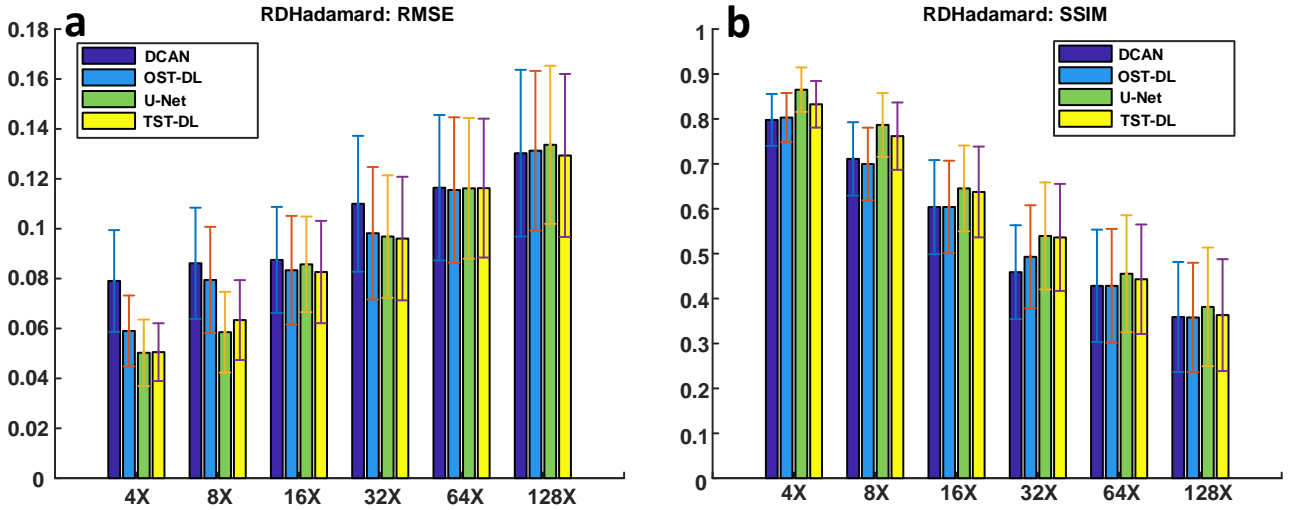


Fig. 3. Quantitative comparison in terms of RMSE and SSIM. (a) RMSE for DCAN, OST-DL, U-Net and TST-DL in all compression ratios with RD Hadamard patterns. (b) SSIM for DCAN, OST-DL, U-Net and TST-DL in all compression ratios with RD Hadamard patterns.

Single-pixel imaging with random Hadamard patterns

In the second case, random Hadamard patterns are used in the single-pixel imaging to test how TST-DL performs in a more challenging case since the reconstruction is more difficult than that from the RD Hadamard patterns³⁹. The random Hadamard patterns were generated in Matlab by randomly permuting a full basis of 4,096 64×64-pixel patterns. The same training, validating and testing images were used here as in the RD Hadamard case. For random Hadamard patterns, we only reconstruct the images at 4X and 8X compression ratios.

Fig. 4 shows representative results at the 4X compression ratio from DCAN, OST-DL, U-Net, TST-DL, and the ground-truth images. Visually, the TST-DL performs better than the other 3 DL frameworks. The fine details of the images can be reconstructed from TST-DL while they are only partially reconstructed or totally lost in other DL frameworks. For instance, in Fig. 4(c₁-c₄), the wheel of the van can be fully reconstructed in TST-DL while it is partially reconstructed in U-Net and totally lost in DCAN, OST-DL.

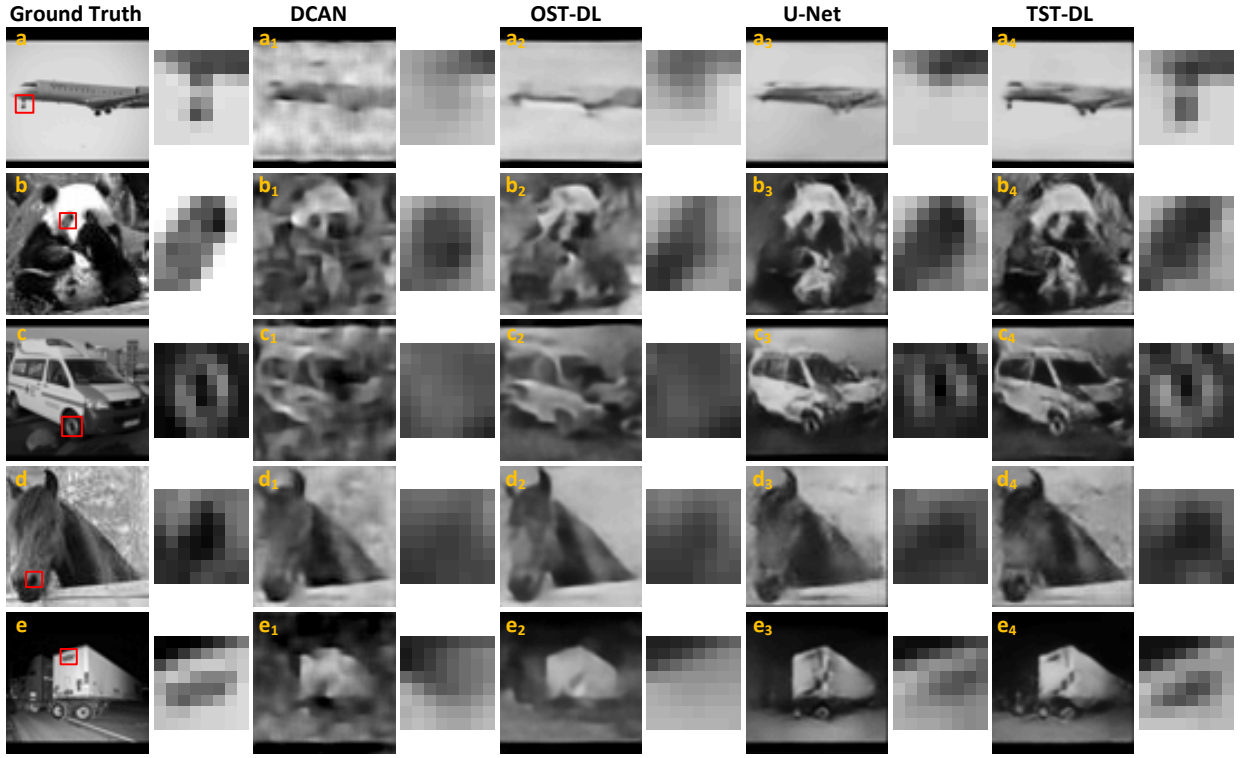


Fig. 4. Five representative reconstructed images in the testing dataset from DCAN, OST-DL, U-Net, TST-DL and some fine details with the random Hadamard patterns at the 4X compression ratio and the ground-truth images. (a) The ground-truth image of an aircraft and the fine detail of the undercarriage. (a₁-a₄) The reconstructed aircraft images from DCAN, OST-DL, U-Net and TST-DL with the fine detail of the undercarriage. (b) The ground-truth image of a panda and the fine detail of the eye. (b₁-b₄) The reconstructed panda images from DCAN, OST-DL, U-Net and TST-DL with the fine detail of the eye. (c) The ground-truth image of a van and the fine detail of the wheel. (c₁-c₄) The reconstructed van images from DCAN, OST-DL, U-Net and TST-DL with the fine detail of the wheel. (d) The ground-truth image of a horse with the fine detail of the nose. (d₁-d₄) The reconstructed horse images from DCAN, OST-DL, U-Net and TST-DL with the fine detail of the nose. (e) The ground-truth image of a truck and the fine detail of the label. (e₁-e₄) The reconstructed truck images from DCAN, OST-DL, U-Net and TST-DL with the fine detail of the label.

To quantitatively compare the results, the mean and the standard deviation of the RMSE and SSIM in the testing dataset were calculated for all the 4 DL frameworks as shown in Supplementary Fig. 1 at 4X and 8X compression ratios. It shows that TST-DL performs better than the other 3 DL frameworks with lower RMSE and higher SSIM. Specifically, TST-DL performs much better than OST-DL since TST-DL learns the model and the optimal regularizer individually while OST-DL learns both simultaneously resulting in an overburden. And interestingly, TST-DL is even better than the U-Net approach which requires the knowledge of the model for an initial guess of the image. The reason is that the random Hadamard matrix is less coherent than RD Hadamard matrix so that the initial guess of the image does not include key features in the image. Thus, we expect that as the information-preserving ability of the forward model degrades, the TST-DL approach will further improve.

PA imaging with a linear array ultrasound transducer

PA imaging with a linear array ultrasound transducer is used as a third case to prove that TST-DL can be applied to a wide range of imaging problems. The details of the system parameters and the training procedures are demonstrated in **Methods**. Fig. 5 shows the reconstructed results from DCAN, OST-DL, LSQR, TwIST, U-Net and TST-DL together with the corresponding input radio-frequency (RF) data and the ground-truth initial pressure distribution (IPD) images. The LSQR approach has the worst results for all the 5 reconstructed images. Specifically, it cannot remove the image artifacts coming from the finite aperture of the linear array ultrasound transducer. The DCAN, OST-DL, TwIST, U-Net and TST-DL have the reasonably good reconstructions for all the 5 images although tiny image mismatch happens.

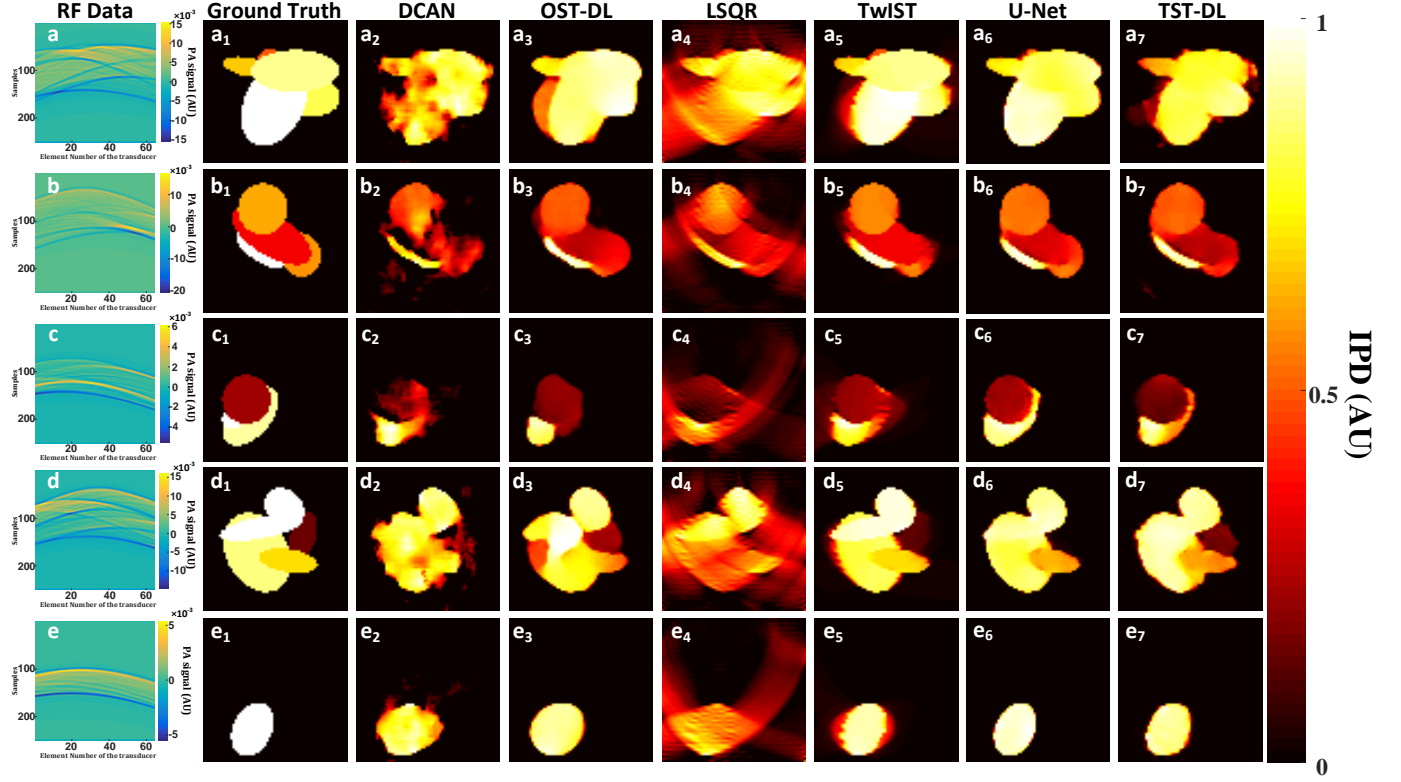


Fig. 5. Five representative reconstructed IPD images (a-e) in the testing dataset from DCAN, OST-DL, LSQR, TwIST, U-Net and TST-DL together with the corresponding RF data and the ground-truth IPD images.

To further quantitatively compare the results, the mean and standard deviation of the RMSE and SSIM for all the reconstructed images in the testing dataset in all the approaches were calculated and shown in Supplementary Fig. 2. Overall, the U-Net demonstrates the best performance compared with other approaches, which is reasonable since the forward operator is known and used for LSQR reconstruction as the input image of U-Net. The LSQR approach has the worst results because of its failure to remove artifacts. For all the approaches without the physics prior of the forward operator, TST-DL performs the best with a lower RMSE and a higher SSIM. Therefore, for real-time PA imaging without physics priors, TST-DL still performs the best.

Noise Robustness

Since noise exists in the measurement data for most of the real cases, different levels of white Gaussian noise (-5dB, 0dB, 5dB, 10dB and 15dB SNR levels) are added to the one-dimensional (1D) measurement data in single-pixel imaging with RD Hadamard patterns at the 4X compression ratio to test the robustness of the TST-DL to noise. The mean and standard deviation of the RMSE and SSIM for all the reconstructed images in the testing dataset at each noise level are calculated to quantitatively compare the performance as shown in Fig. 6 (a). It shows that with the increase of the noise level (decrease of the SNR), the reconstruction performance is dropping with the increase of the RMSE and decrease of the SSIM. However, the results still remain at a reasonable level with the RMSE lower than 0.11 and SSIM larger than 0.50 at the -5dB SNR level. Fig. 6 (b-c) show the 1D measurement data without noise and with -5dB SNR of noise, respectively.

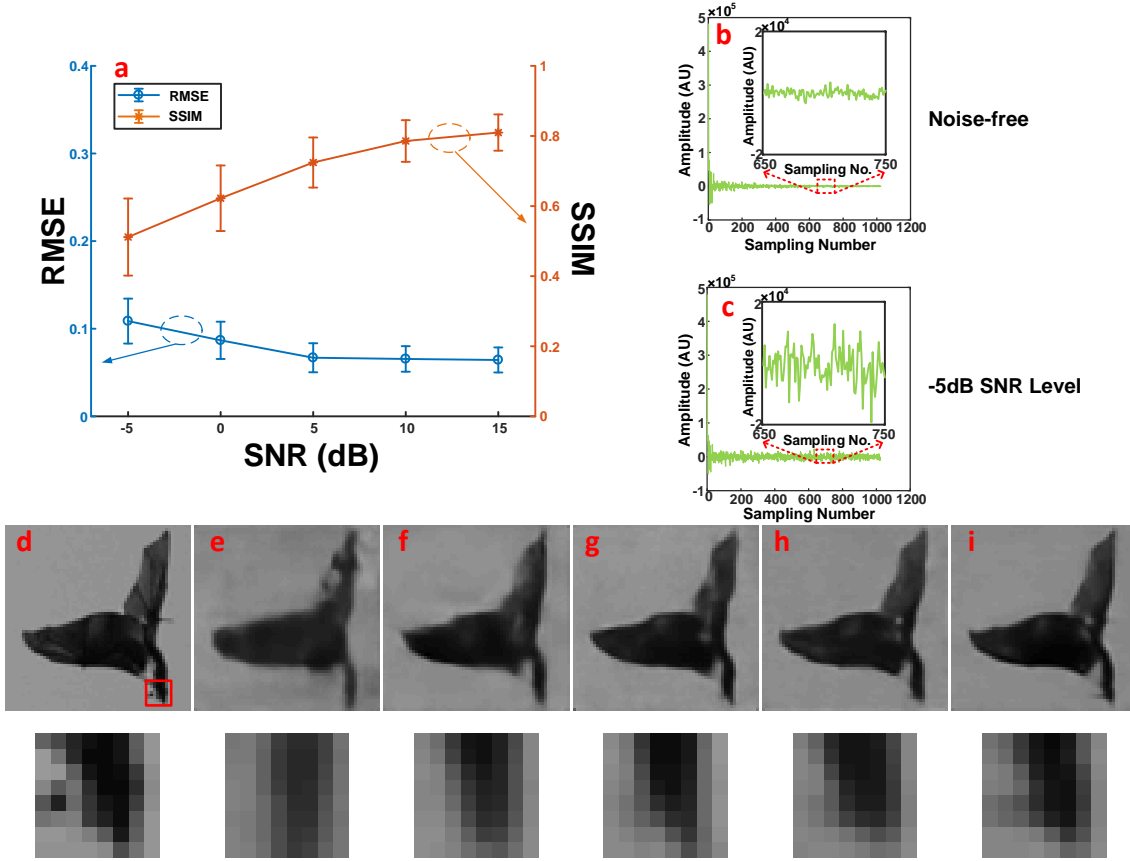


Fig. 6 Noise robustness test. (a) RMSE and SSIM of the TST-DL results at the -5dB, 0dB, 5dB, 10dB and 15dB SNR levels. (b) 1D measurement data without noise. (c) 1D measurement data at the -5dB SNR level. (d) The ground-truth of an image in the testing dataset and the fine detail in the red square. (e) The TST-DL prediction of the image and the fine detail in (d) at the -5dB SNR level. (f) The TST-DL prediction of the image and the fine detail in (d) at the 0dB SNR level. (g) The TST-DL prediction of the image and the fine detail in (d) at the 5dB SNR level. (h) The TST-DL prediction of the image and the fine detail in (d) at the 10dB SNR level. (i) The TST-DL prediction of the image and the fine detail in (d) at the 15dB SNR level.

Fig. 6 (e-i) show the reconstructed images at -5dB, 0dB, 5dB, 10dB and 15dB SNR levels with the same ground-truth image in Fig. 6 (d). Although the reconstructed images become more and more blurred with the increase of the noise, the general shape and even some of the details (the mouth of the bird in the zoom-in figures) can still be well reconstructed at the 0dB, 5dB, 10dB and 15dB SNR levels. Given the SNR levels at -5dB, 0dB, 5dB are extremely high levels of noise (for 0dB, the noise level is the same as the signal level), we can conclude that TST-DL is robust to noise.

Reducing the size of the training dataset

Because a large training dataset is not always available for real cases, the size of the training dataset is also a key factor in DL frameworks. Therefore, we test the impact of the size of the training dataset in the TST-DL to find a reasonable size of the training dataset while still maintaining good reconstruction results.

Fig. 7 (a) shows the TST-DL performance of the prediction in the same testing dataset with the RD Hadamard patterns at the 4X compression ratio in terms of RMSE and SSIM with 625, 1,250, 2,500, 5,000 and 10,000 training images. The results show that with the decrease of the number of training samples, the TST-DL performance drops but still remains reasonably good at the case of 2,500 training images. Fig. 7 (c-g) show the reconstruction results of the same image in the testing dataset with 625, 1,250, 2,500, 5,000 and 10,000 training images respectively together with the ground-truth image in Fig. 7 (b). The image becomes clearer and the detail is better reconstructed with the increase of the number of training samples. Qualitatively, the case of 2,500 training images has a reasonably good reconstruction result, which is consistent with the quantitative results in Fig. 7 (a). Overall, with these results, it can be proved that TST-DL can still perform well with a small training dataset which means that it can be applicable to many real image reconstruction cases where a large training dataset is not available.

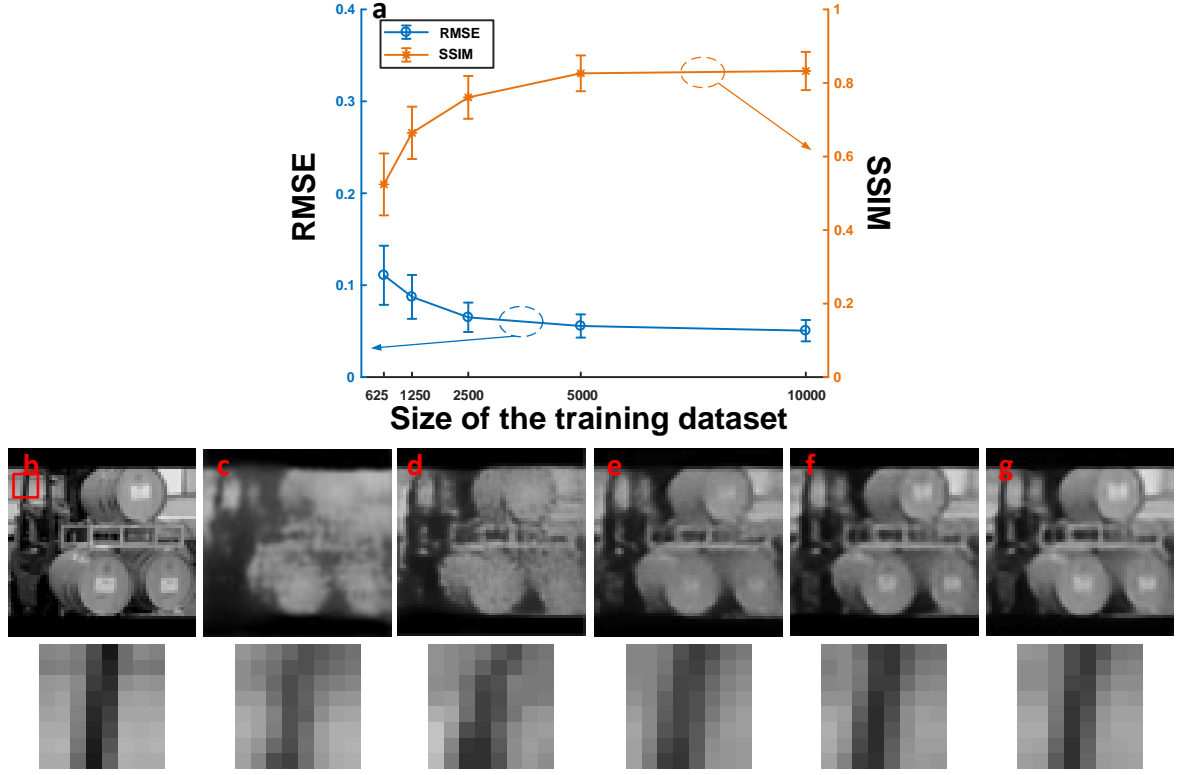


Fig. 7. Reducing the size of the training dataset. (a) The RMSE and SSIM of the TST-DL results with 625, 1,250, 2,500, 5,000 and 10,000 training images. (b) The ground truth of the oil-tank image in the testing dataset and fine detail in the red square; (c) The TST-DL prediction of the image and the fine detail in (b) with 625 training images. (d) The TST-DL prediction of the image and the fine detail in (b) with 1,250 training images. (e) The TST-DL prediction of the image and fine detail in (b) with 2,500 training images. (f) The TST-DL prediction of the image and the fine detail in (b) with 5,000 training images. (g) The TST-DL prediction of the image and the fine detail in (b) with 10,000 training images.

Image de-autocorrelation

For all the above reconstruction cases, the imaging model is linear such that the forward operator can be described as a 2D matrix. Thus, the forward model and its inverse can both be implemented in matrix multiplication. TST-DL has proven effective at handling these imaging models since the FCL in the first-step training corresponds to matrix multiplication. Here, we extend the utility of TST-DL to handle nonlinear imaging models which cannot be described as matrix multiplication. Image autocorrelation is a nonlinear model such that the inverse process, image de-autocorrelation is also a nonlinear process. One of the important applications of image de-autocorrelation is to reconstruct the image through scattering medium²⁹ by solving a phase-retrieval problem from the Fourier-domain magnitude measurement^{40,41}. Therefore, we apply TST-DL to the image de-autocorrelation problem as a test case for the nonlinear model. In order to handle nonlinear models, a slight modification is made to TST-DL by using 3 FCLs connected in series instead of a single FCL in the first-step training. More FCLs with a nonlinear activation function will add more nonlinearity to the DL networks to handle the nonlinear imaging problems. The details of the training procedures are demonstrated in **Methods**.

Previously²⁹, the image de-autocorrelation was achieved through phase-retrieval algorithms. Therefore, we compare the results with those from the Gerchberg-Saxton phase-retrieval algorithm⁴⁰. Fig. 8 shows the reconstruction results with images in Fig. 8 (a-j) to be the autocorrelation images, Fig. 8 (a₁-j₁) to be the ground-truth images, Fig. 8 (a₂-j₂) to be the reconstructed images from the phase-retrieval algorithm, Fig. 8 (a₃-j₃) to be the intermediate reconstructed images from the first-step training in TST-DL and Fig. 8 (a₄-j₄) to be the reconstructed images from the TST-DL. From the results, we can find that the phase-retrieval algorithm sometimes fails to work because of twinned image artifacts in the reconstructed images while TST-DL is much more robust. For further quantitative comparison, the RMSE and SSIM were calculated. The RMSE for all the reconstructed images in the testing dataset is 0.137 for TST-DL and 0.155 for

the phase-retrieval algorithm. The corresponding SSIM is 0.815 for TST-DL and 0.735 for the phase-retrieval algorithm. Therefore, TST-DL has a more stable reconstruction than the phase-retrieval algorithm and performs better in terms of RMSE and SSIM. It also means that TST-DL is able to handle nonlinear inverse imaging problems with a slight modification.

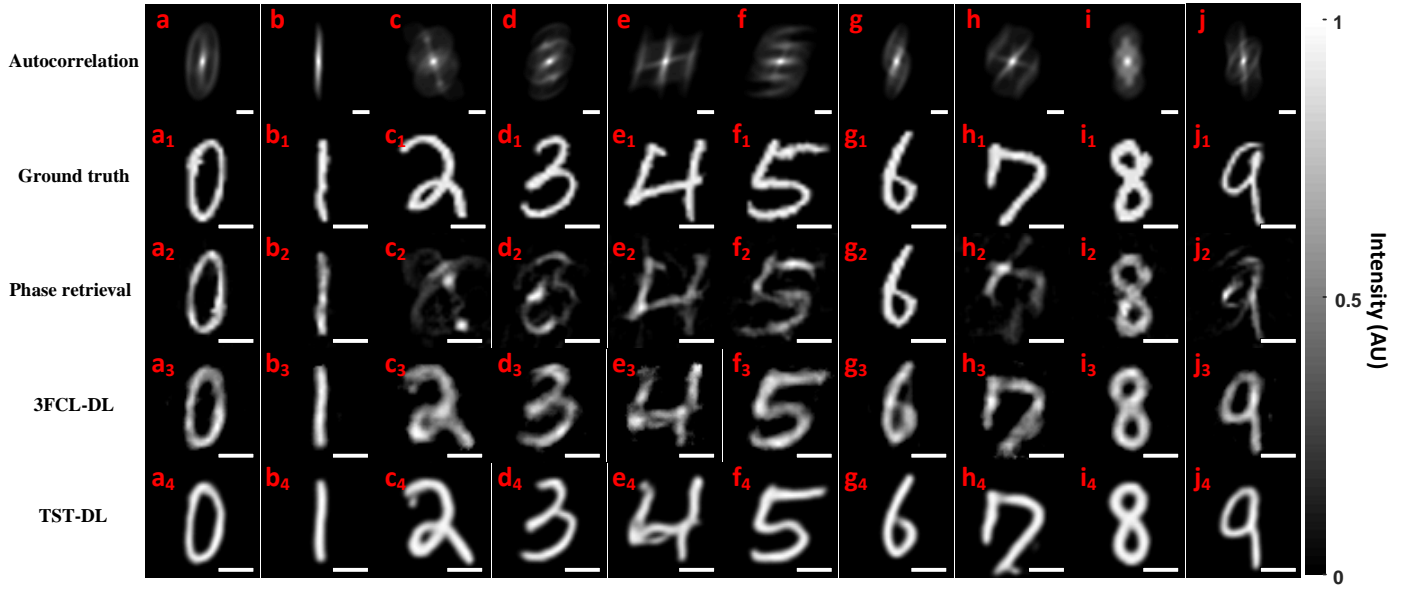


Fig. 8. Image de-autocorrelation results of ten representative images in the testing dataset from MNIST. (a-j) Autocorrelated images. (a₁-j₁) Ground-truth images. (a₂-j₂) Reconstructed images from the phase-retrieval algorithm. (a₃-j₃) Intermediate reconstructed images from the first-step training in TST-DL. (a₄-j₄) Reconstructed images from TST-DL. The scale bar denotes 20 pixels.

Experimental single-pixel imaging with random grayscale patterns

The experimentally recorded data in single-pixel imaging with random grayscale illumination patterns is used to verify the effectiveness of TST-DL in experimental single-pixel imaging. Since TST-DL and OST-DL perform better than DCAN in the approaches without the physics priors, and U-Net performs better than TwIST and LSQR in the approaches with the physics priors, we only test and compare TST-DL, OST-DL and U-Net with the experimental data. The system and training procedures are demonstrated in **Methods**.

The results are shown in Fig. 9. Fig. 9 (a-j) shows 10 ground-truth images for testing. Fig. 9 (a₁-j₁), (a₂-j₂) and (a₃-j₃) show the reconstructed images from OST-DL, U-Net and TST-DL at 4X compression ratio. Fig. 9 (a₄-j₄), (a₅-j₅) and (a₆-j₆) show the reconstructed images from the three DL approaches at 20X compression ratio. Quantitative comparison is made by calculating the RMSE and SSIM between the reconstructed images and the ground-truth images as shown in Supplementary Table 2. It shows that TST-DL still outperforms OST-DL in terms of RMSE and SSIM at both 4X and 20X compression ratios. Thus, it is seen in the experiment that TST-DL can overcome the overburdening issue (learning the model and the optimal regularizer simultaneously) in the established end-to-end DL approaches by learning the model and the optimal regularizer individually. At 4X compression ratio, U-Net performs a little better than TST-DL since the forward model is known as the physic prior for the initial LSQR image reconstruction as the U-Net input. At 20X compression ratio, TST-DL performs better than U-Net since the initial LSQR image reconstruction at 20X has a bad image quality so that as the input of U-Net, it does not provide much image information.

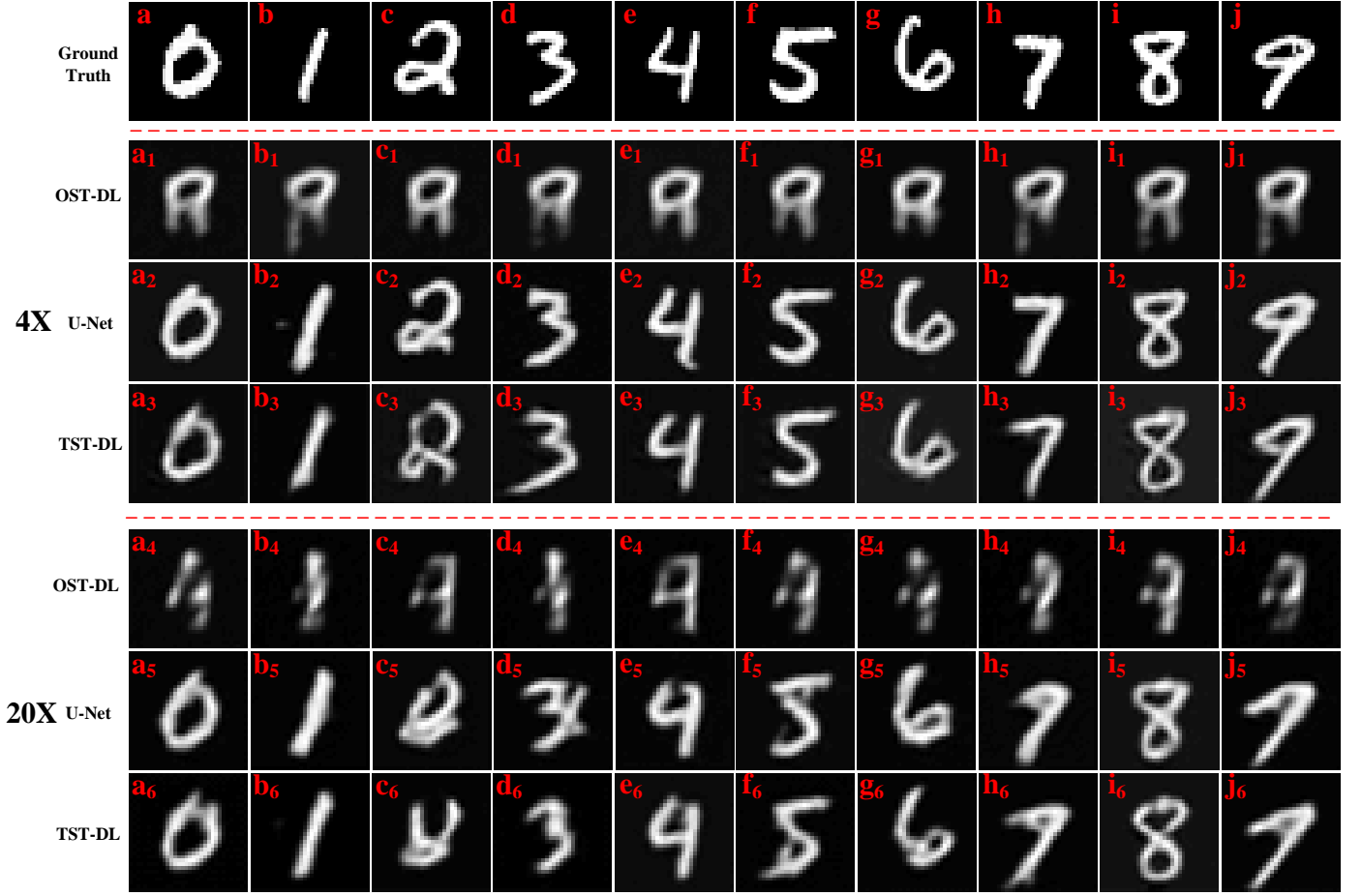


Fig. 9 Experimental results on single-pixel imaging with 4X and 20X compression ratios. (a-j) Ground-truth images. (a₁-j₁) Reconstructed images from OST-DL at 4X compression ratio. (a₂-j₂) Reconstructed images from U-Net at 4X compression ratio. (a₃-j₃) Reconstructed images from TST-DL at 4X compression ratio. (a₄-j₄) Reconstructed images from OST-DL at 20X compression ratio. (a₅-j₅) Reconstructed images from U-Net at 20X compression ratio. (a₆-j₆) Reconstructed images from TST-DL at 20X compression ratio.

Experimental PA imaging with a linear array ultrasound transducer

As a second experimental case, we apply the method to our experiment PA imaging system. The impulse-response RF signals in PA imaging of the single graphite rod were collected as the training dataset in the experiment using previously published methods⁷. The system and training data collection are demonstrated in **Methods**. Supplementary Fig. 3 (a-c) show the three representative IPD images as the output of the TST-DL network for training and Supplementary Fig. 3 (d-f) show their corresponding impulse-response RF signals as the input of the TST-DL network for training after vectorization. The noise in the RF signals in Supplementary Fig. 3 (d-f) is from the extra reflection in the medium.

The RF signals from a polyacrylamide tissue-mimicking phantom⁴² as mentioned in Sec. 4.2 and Fig. 6 (a-c) in⁷ are used as the testing dataset for TST-DL prediction. This tissue-mimicking phantom contains two 0.2-mm diameter graphite rods and dissolved 7 mg of the titanium dioxide for a concentration of 0.035mg/ml to mimic the same scattering effect as in the impulse response measurement experiment. Since the back-projection (a non-iterative reconstruction approach) and TwIST (an iterative reconstruction approach) approaches perform well in reconstructing point objects⁷, we use their results as an indication of the ground truth (or close to the ground truth since errors occur sometimes). And since TST-DL outperforms the other non-physics-priors DL frameworks in all the simulations, we only compare the TST-DL with back-projection and TwIST. In addition, since the RF signal of the tissue-mimicking phantom (the testing dataset) has higher level of noise than that from the impulse-response RF signal (the training dataset) because of the medium difference, the TST-DL prediction will have some noise on the background. Therefore, a threshold of 0.5 is applied to the TST-DL predicted images after normalization as well as to the back-projection and TwIST results (any pixel value less than or equal to 0.5 will be set to 0).

Fig. 10 shows the experimental reconstructed results on the tissue-mimicking phantom at 4 scanning locations. Fig. 10 (a₁-d₁) show the RF data at the 4 scanning locations. Fig. 10 (a₂-d₂) show the reconstructed IPD images from the back-projection approach as a non-iterative reconstruction approach. Fig. 10 (a₃-d₃) show the reconstructed IPD images from TwIST as an iterative reconstruction approach. Fig. 10 (a₄-d₄) show the reconstructed IPD images from TST-DL. Ideally, there should be only two points in the reconstructed IPD images since the diameter of the two graphite rods in the phantom is smaller than the resolution of the reconstructed images. The extra non-zero signal in the reconstructed IPD images might be from the extra reflection in the phantom. Compared with the ground-truth IPD images from the back-projection and TwIST approaches, TST-DL predicts the points at the correct location with high precision. Especially for the reconstructed IPD images from the RF data in Fig. 10 (d₁), pointed by the green arrows, there is supposed to be only one absorber reconstructed at the location as shown in Fig. 10 (d₄) from TST-DL while two absorbers are reconstructed in both back-projection and TwIST images in Fig. 10 (d₂) and Fig. 10 (d₃). Therefore, TST-DL can be proved to be a reliable image reconstruction tool in real PA experiments.

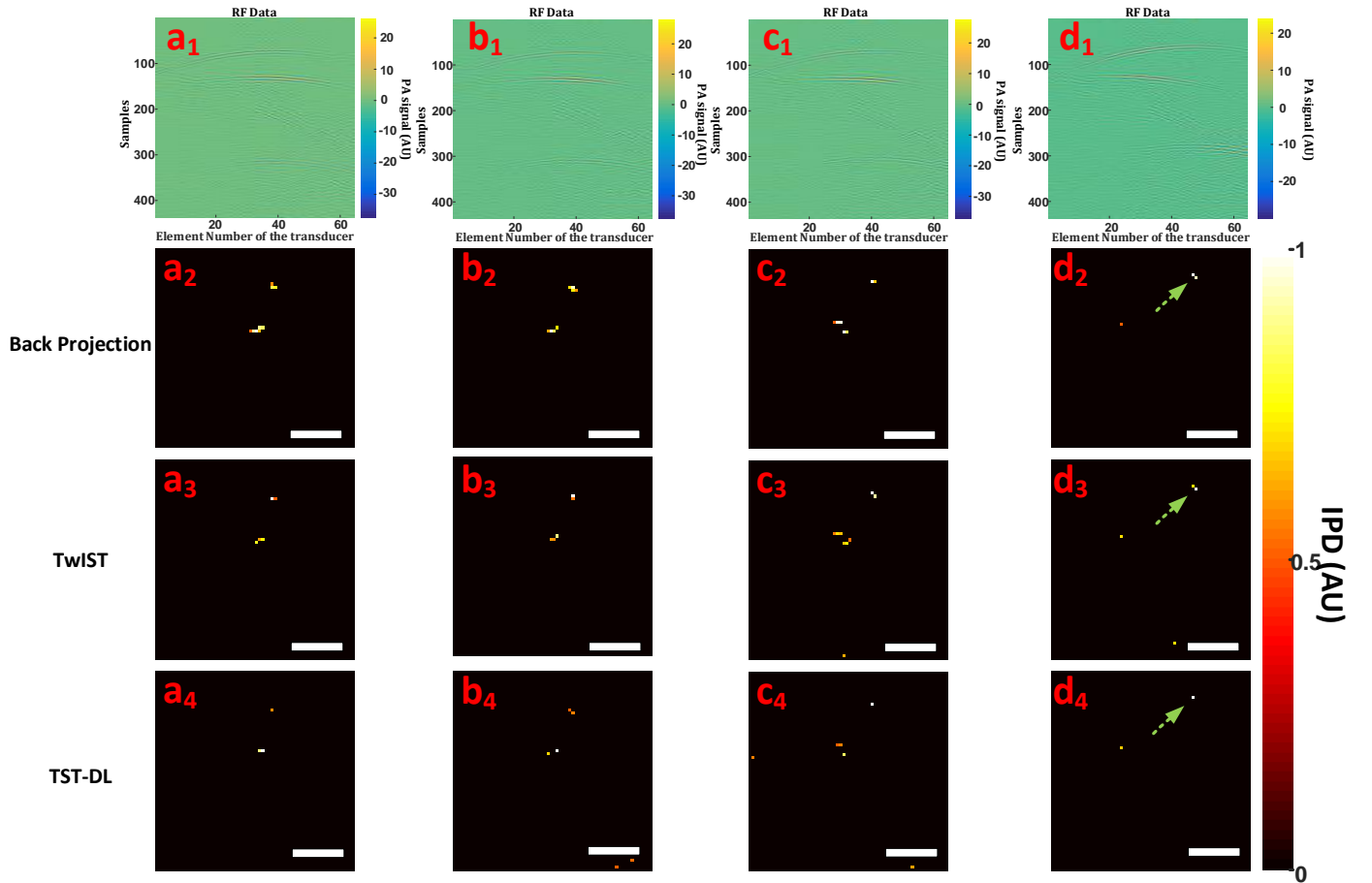


Fig. 10. Experimental results on tissue-mimicking phantom reconstruction. (a₁-d₁) The RF data at 4 scanning locations. (a₂-d₂) Reconstructed IPD images from the back-projection approach. (a₃-d₃) Reconstructed IPD images from TwIST. (a₄-d₄) Reconstructed IPD images from TST-DL. The green arrows point to the absorber(s) at one location reconstructed from the RF data in (d₁) using back-projection, TwIST and TST-DL. The scale bar denotes 5mm.

DISCUSSION

In conclusion, a TST-DL framework is proposed for real-time computational imaging without prior knowledge of the imaging model while handling the input-output image size- and dimensionality- mismatch issues. The FCL in the first-step training directly learns the inverse of the forward operator given the training data. Then, the pre-trained FCL is fixed and concatenated with a U-Net for a second-step training as a regularization step. Four simulations and two experiments with different imaging models were conducted to verify the effectiveness of the proposed TST-DL with quantitative comparison with other DL frameworks and the iterative model-based optimization approaches. The

averaged time to predict an image from the testing dataset in TST-DL is $\leq 1\text{ms}$ in the simulations. The results show the TST-DL outperforms the other DL frameworks without physics priors and is comparable to (and sometimes better than) the DL framework and iterative optimization approaches that incorporate the known forward operator.

Although the TST-DL framework shows superior performance in these studies, there are still some trade-offs in the framework. A relatively large number of the training data is needed to optimize the parameters since the FCL is used to directly learn the model in the first step of TST-DL and it has a large number of parameters to train. Therefore, obtaining enough training samples in the real experiment for training is still a challenging issue although the problem occurs in most DL frameworks. In addition, training a large number of parameters also requires a significant amount of memory such that a powerful computer (such as a workstation) is a requirement while the commonly used DL frameworks with convolutional neural networks is applicable in a normal desktop with lower power requirement. Besides, since a combination of DSSIM and RMSE is used as the loss function in the second-step training, the ratio between DSSIM and RMSE still needs to be determined heuristically based on the training dataset. Moreover, although it is proved that TST-DL can also reconstruct the images in nonlinear imaging models, further exploration is still needed in determining the optimal number of FCLs to use and the choose of the nonlinear activation functions in each FCL.

We believe that TST-DL has two main contributions to the DL field. First, it provides a DL framework that can be applied to virtually any imaging modality. Second, it provides a reliable real-time DL approach for imaging modalities where the physics priors are difficult to acquire with high accuracy, unknown or even nonlinear, and overcomes the overburdening issue from the established end-to-end DL approaches by introducing the two-step-training strategy. Therefore, we believe that TST-DL will further improve the impact of DL in the imaging field.

METHODS

Regularized optimization. Any imaging model can be described by

$$g = \mathbf{H}f \quad (1)$$

where f is the image to be reconstructed, g is the raw measurement data and \mathbf{H} is the forward operator.

The most straightforward way to reconstruct the image f is to find the inverse of the forward operator \mathbf{H}^{-1} so that $\mathbf{H}^{-1}\mathbf{H} = \mathbf{I}$ where \mathbf{I} is the identity matrix. However, for most of the cases, \mathbf{H}^{-1} is not unique or requires excessive computational power to determine.

An effective alternative to directly computing the inverse of the forward model is to iteratively solve the optimization problem,

$$\hat{f} = \underset{f}{\operatorname{argmin}} \|\mathbf{H}f - g\|_2^2 \quad (2)$$

where $\|\cdot\|_2$ denotes the L_2 norm. However, this pseudo-inverse solution is prone to artifacts and noise due to the ill-posed property of the forward operator \mathbf{H} . Therefore, additional information is needed to converge to the correct solution.

A regularized optimization approach can incorporate additional knowledge about the image by adding a regularization term,

$$\hat{f} = \underset{f}{\operatorname{argmin}} \{\|\mathbf{H}f - g\|_2^2 + \lambda\phi(f)\} \quad (3)$$

where ϕ is the regularization operator and λ is the regularization parameter. $\|\mathbf{H}f - g\|_2^2$ is the fidelity term and $\phi(f)$ is the regularization term. The regularization term is to make a balance with the fidelity term by driving the optimized \hat{f} to match a specific regularization rule. The common regularization domains include spatial, edge, or wavelet domains and so on. However, finding the optimal regularization rule for a specific image dataset is still a challenging problem¹⁵.

Inspired by the regularized optimization approach, we propose TST-DL framework. The first-step training is to train a FCL to learn an optimal \mathbf{H}^{-1} (assuming \mathbf{H} is a linear operator) given the training datasets (g, f) . Then, this pre-trained FCL is fixed and concatenated with a U-Net for the second-step training to learn an optimal regularization rule to regularize f towards the optimal solution. We further extend this concept to nonlinear models by using multiple FCLs to learn the optimal nonlinear operator \mathbf{H}^{-1} .

The TST-DL parameters. The mean squared error (MSE) is used as the loss function in the first-step training to find the optimal \mathbf{H}^{-1} that minimizes $\|f - \mathbf{H}^{-1}g\|_2^2$. A customized loss function with a combination of RMSE and difference of structural similarity index (DSSIM) is used for the second-step training. The default learning rate is used. The batch size is chosen to be 50 and each training step runs 100 epochs. Dropout layers (not shown in Fig. 1) are used in the second step (U-Net) of TST-DL to prevent overfitting issues.

Usage of DCAN, U-Net and OST-DL. The DCAN is developed in single-pixel imaging to reconstruct the dynamic scenes from the single-pixel camera capture of the compressed signal. DCAN is comprised of two parts, the encoding part to find the optimal binary filters for the measurement and the decoding part for image reconstruction with FCL and three convolutional layers³⁶. We only use the decoding part in DCAN since the binary filters as the physics priors are unknown. For the U-Net approach, an initial guess of the image is reconstructed using the LSQR approach. Then, the initial guess of the image is used as the input of U-Net for further training and prediction. For OST-DL, as an end-to-end DL approach, the FCL is concatenated with U-Net for a one-step training to learn the model and the optimal regularizer simultaneously instead of training each individually. For DCAN and OST-DL, both as one-step training approaches, the training runs 200 epochs for a fair comparison with TST-DL. For U-Net, since the initial guess of the image is obtained because of the known forward model, the training runs 100 epochs for a fair comparison with TST-DL.

Training procedures in single-pixel imaging with RD Hadamard patterns. The STL-10 natural image database ³⁷ was used for training the TST-DL framework with 10,000 images as the training dataset, 2,000 images as the validating dataset and another 2,000 images as the testing dataset. In order to meet the dimension requirement of the RD Hadamard patterns, all the images were down-sampled from 96×96 to 64×64 . The full RD Hadamard basis for a 64×64 image has 4,096 RD Hadamard patterns each with a size of 64×64 . Different compression ratios were used here as 4X, 8X, 16X, 32X, 64X and 128X, corresponding to taking the first 1/4, 1/8, 1/16, 1/32, 1/64, and 1/128 of RD Hadamard patterns, respectively. For instance, in 4X compression, the first 1,024 RD Hadamard patterns were used. The 1D raw measurement data was acquired by multiplying each individual image with the RD Hadamard patterns at each compression ratio. Therefore, the 1D raw measurement data has a size of $1,024 \times 1$, 512×1 , 256×1 , 128×1 , 64×1 and 32×1 for the corresponding compression ratios.

Training procedures in simulated PA imaging. 9,000 PA objects were simulated as the ground-truth IPD images with random number of oval objects randomly located in the field of view (FOV) similar to the blood vessel cross-sections one would encounter in biomedical PA imaging. These objects have random intensities ranging from 0 to 1. The size of each image is 64×64 . The k-Wave toolbox ⁴³ was used to simulate the corresponding RF data with a simulated 64-element linear array ultrasound transducer (0.15mm pitch size) oriented horizontally on top of the object to be imaged. A sampling frequency of 22 MHz and a center frequency of 6 MHz with a bandwidth of 4.8 MHz was used. After the simulation, we vectorized the 2D RF data as the input of DCAN, OST-DL and TST-DL. We used 5,000 RF datasets and the corresponding ground-truth IPD images as the training dataset, 2,000 RF data and the corresponding ground-truth IPD images as the validating dataset, and 2,000 RF data and the corresponding ground-truth IPD images as the testing dataset. For the U-Net, the IPD images from LSQR approach were used as the input images and the corresponding ground-truth IPD images as the output images. The established model-based iterative optimization approaches (LSQR and TwIST) were also included to reconstruct 200 IPD images in the testing dataset for comparison.

Training procedures in image de-autocorrelation. The handwriting numbers in the MNIST database ⁴⁴ were used as the ground-truth images. The raw images in MNIST were resized from 28×28 to 64×64 pixels. 10,000 images from the training dataset in MNIST were used as the training dataset, 2,000 images from the testing dataset in MNIST were used as the validating dataset and another 2,000 images from the testing dataset in MNIST were used as the testing dataset. Then, the image autocorrelation was applied to each of the images. The vectorized autocorrelated images were used as the input of TST-DL and their corresponding ground-truth images were used as the output of the network to achieve image de-autocorrelation. Each step in TST-DL ran 50 epochs.

The system and training procedures in experimental single-pixel imaging. The objects images were taken from MNIST database ⁴⁴ and resized from 28×28 to 32×32 pixels. 1,024 random grayscale illumination patterns each with a size of 32×32 were prepared as the full basis. Then, the first 51 and 256 illumination patterns in the full basis were used to illuminate the objects respectively, corresponding to a 20X and 4X compression ratio respectively. Therefore, the corresponding 1D raw measurement data has a size of 51×1 and 256×1 respectively (The 1D raw measurement data with the full illumination patterns has a size of $1,024 \times 1$). TST-DL and OST-DL were trained with 200 images in the training dataset of MNIST and their corresponding simulated 1D measurement data at the two compression ratios respectively and tested on the experimentally acquired 1D measurement data of 10 images in MNIST database different from the 200 training images. In U-Net, the reconstructed images from LSQR approach were used as the network input instead of the 1D measurement data for both training and testing cases. The batch size was chosen to be 10 since only 200 images and the corresponding 1D raw measurement data were trained. The imaging system is shown in Fig. 10 in ⁴⁵ and in Fig. 4 in ⁴⁶. Each testing image was printed on a paper card and illuminated by the same patterns as in the simulation from a JmGO G3 projector. The 1D measurement data was recorded by a Thorlabs FDS1010 photodiode detector and a NI USB-6216 data acquisition card.

The system for training data collection in experimental PA imaging. A 0.2-mm diameter graphite rod was immersed into water with its cross section to be used as the point source for the impulse response measurements. Then, 0.035 mg/ml of titanium dioxide was added into water as scatterers to mimic the scattering effects in the real biological tissues. 7-ns laser pulses at a 10-Hz repetition rate ($\lambda = 770$ nm) from an Nd:YAG 2nd harmonic pumped optical parametric oscillator (OPO) laser system (Phocus Mobile HE, Opotek Inc.) was used to illuminate the graphite rod. The PA signal from the optical absorption in the graphite was acquired simultaneously by the 128 elements of a linear array ultrasound transducer (L11-4V, Verasonics, pitch size 0.3mm) connected to a Verasonics Vantage 256 ultrasound imaging system (sampling frequency 22.7MHz) ⁷. A 2D stepper motor was used to move the graphite rod in lateral and axial directions to measure the impulse responses at different locations in the FOV. For the purpose of shortening experimental time as mentioned in ⁷, only the RF dataset of the impulse response from 64×64 points in the FOV were collected with only 64 elements of the ultrasound transducer. Therefore, a total of 4,096 impulse responses were collected. Then, these impulse responses were reordered in a random order and vectorized individually, and the first 3,200 of them and their corresponding IPD images were taken as the training dataset. All the layers from the first-step training were fixed in the second-step training in this experimental PA imaging. The first step in TST-DL ran 100 epochs and the second step in TST-DL ran 50 epochs.

ACKNOWLEDGMENTS

This work is supported by a Faculty Grant from the Neukom Institute for Computational Science at Dartmouth College. We thank Dr. Shuming Jiao and Miss Jun Feng (Nanophotonics Research Center, Shenzhen University, China) for providing experimental data of single-pixel imaging.

AUTHOR CONTRIBUTIONS

R.S. designed and built the TST-DL network structure, designed and carried out all the simulations and the PA imaging experiment, analyzed the data and wrote the paper. K.H.H helped to build the TST-DL network structure. G.P.L helped to design the TST-DL network structure, all the simulations and PA imaging experiment, and edited the manuscript.

COMPETING FINANCIAL INTERESTS

The authors declare no conflicts of interest.

REFERENCES

1. Mait JN, Euliss GW, Athale RA. Computational imaging. *Advances in Optics and Photonics* **10**, 409-483 (2018).
2. Barbastathis G, Ozcan A, Situ G. On the use of deep learning for computational imaging. *Optica* **6**, 921-943 (2019).
3. Candes E, Romberg J. Sparsity and incoherence in compressive sampling. *Inverse problems* **23**, 969 (2007).
4. Candès EJ, Wakin MB. An introduction to compressive sampling [a sensing/sampling paradigm that goes against the common knowledge in data acquisition]. *IEEE signal processing magazine* **25**, 21-30 (2008).
5. Gao L, Liang J, Li C, Wang LV. Single-shot compressed ultrafast photography at one hundred billion frames per second. *Nature* **516**, 74 (2014).
6. Wang Z, *et al.* Compressive holographic video. *Optics express* **25**, 250-262 (2017).
7. Shang R, Archibald R, Gelb A, Luke GP. Sparsity-based photoacoustic image reconstruction with a linear array transducer and direct measurement of the forward model. *Journal of biomedical optics* **24**, 031015 (2018).
8. LeCun Y, Bengio Y, Hinton G. Deep learning. *nature* **521**, 436 (2015).
9. Rivenson Y, Göröcs Z, Günaydin H, Zhang Y, Wang H, Ozcan A. Deep learning microscopy. *Optica* **4**, 1437-1443 (2017).
10. Rivenson Y, Zhang Y, Günaydin H, Teng D, Ozcan A. Phase recovery and holographic image reconstruction using deep learning in neural networks. *Light: Science & Applications* **7**, 17141 (2018).
11. Li Y, Xue Y, Tian L. Deep speckle correlation: a deep learning approach toward scalable imaging through scattering media. *Optica* **5**, 1181-1190 (2018).
12. Xue Y, Cheng S, Li Y, Tian L. Reliable deep-learning-based phase imaging with uncertainty quantification. *Optica* **6**, 618-629 (2019).
13. Sinha A, Lee J, Li S, Barbastathis G. Lensless computational imaging through deep learning. *Optica* **4**, 1117-1125 (2017).
14. Goy A, Arthur K, Li S, Barbastathis G. Low photon count phase retrieval using deep learning. *Physical review letters* **121**, 243902 (2018).

15. Liu J, He Q, Luo J. A compressed sensing strategy for synthetic transmit aperture ultrasound imaging. *IEEE transactions on medical imaging* **36**, 878-891 (2016).
16. Ronneberger O, Fischer P, Brox T. U-net: Convolutional networks for biomedical image segmentation. In: *International Conference on Medical image computing and computer-assisted intervention*. Springer (2015).
17. Chen W, *et al.* Prostate segmentation using 2D bridged U-net. In: *2019 International Joint Conference on Neural Networks (IJCNN)*. IEEE (2019).
18. Shah S, Ghosh P, Davis LS, Goldstein T. Stacked U-Nets: a no-frills approach to natural image segmentation. *arXiv preprint arXiv:1804.10343*, (2018).
19. Chen J, Yang L, Zhang Y, Alber M, Chen DZ. Combining fully convolutional and recurrent neural networks for 3d biomedical image segmentation. In: *Advances in neural information processing systems* (2016).
20. Sun T, Chen Z, Yang W, Wang Y. Stacked U-Nets With Multi-Output for Road Extraction. In: *CVPR Workshops* (2018).
21. Antholzer S, Haltmeier M, Schwab J. Deep learning for photoacoustic tomography from sparse data. *Inverse problems in science and engineering* **27**, 987-1005 (2019).
22. Waibel D, Gröhl J, Isensee F, Kirchner T, Maier-Hein K, Maier-Hein L. Reconstruction of initial pressure from limited view photoacoustic images using deep learning. In: *Photons Plus Ultrasound: Imaging and Sensing 2018*. International Society for Optics and Photonics (2018).
23. Zhang G, *et al.* Fast phase retrieval in off-axis digital holographic microscopy through deep learning. *Optics express* **26**, 19388-19405 (2018).
24. Schwab J, Antholzer S, Nuster R, Paltauf G, Haltmeier M. Deep Learning of truncated singular values for limited view photoacoustic tomography. In: *Photons Plus Ultrasound: Imaging and Sensing 2019*. International Society for Optics and Photonics (2019).
25. Guan S, Khan A, Sikdar S, Chitnis P. Fully Dense UNet for 2D sparse photoacoustic tomography artifact removal. *IEEE journal of biomedical and health informatics*, (2019).
26. Popoff S, Lerosey G, Carminati R, Fink M, Boccarda A, Gigan S. Measuring the transmission matrix in optics: an approach to the study and control of light propagation in disordered media. *Physical review letters* **104**, 100601 (2010).
27. Kim M, Choi W, Choi Y, Yoon C, Choi W. Transmission matrix of a scattering medium and its applications in biophotonics. *Optics express* **23**, 12648-12668 (2015).
28. Wang F, Wang H, Wang H, Li G, Situ G. Learning from simulation: An end-to-end deep-learning approach for computational ghost imaging. *Optics express* **27**, 25560-25572 (2019).
29. Katz O, Heidmann P, Fink M, Gigan S. Non-invasive single-shot imaging through scattering layers and around corners via speckle correlations. *Nature photonics* **8**, 784 (2014).
30. Paige CC, Saunders MA. LSQR: An algorithm for sparse linear equations and sparse least squares. *ACM Transactions*

on *Mathematical Software (TOMS)* **8**, 43–71 (1982).

31. Bioucas-Dias JM, Figueiredo MA. A new TwIST: Two-step iterative shrinkage/thresholding algorithms for image restoration. *IEEE Transactions on Image processing* **16**, 2992–3004 (2007).
32. Sun M-J, Meng L-T, Edgar MP, Padgett MJ, Radwell N. A Russian Dolls ordering of the Hadamard basis for compressive single-pixel imaging. *Scientific reports* **7**, 3464 (2017).
33. Xu M, Wang LV. Photoacoustic imaging in biomedicine. *Review of scientific instruments* **77**, 041101 (2006).
34. Wang LV, Hu S. Photoacoustic tomography: in vivo imaging from organelles to organs. *science* **335**, 1458–1462 (2012).
35. Wang X, Pang Y, Ku G, Xie X, Stoica G, Wang LV. Noninvasive laser-induced photoacoustic tomography for structural and functional in vivo imaging of the brain. *Nature biotechnology* **21**, 803 (2003).
36. Higham CF, Murray-Smith R, Padgett MJ, Edgar MP. Deep learning for real-time single-pixel video. *Scientific reports* **8**, 2369 (2018).
37. Coates A, Ng A, Lee H. An analysis of single-layer networks in unsupervised feature learning. In: *Proceedings of the fourteenth international conference on artificial intelligence and statistics* (2011).
38. Wang Z, Bovik AC, Sheikh HR, Simoncelli EP. Image quality assessment: from error visibility to structural similarity. *IEEE transactions on image processing* **13**, 600–612 (2004).
39. Limbach J, Eisele C, Paunescu G. Analysis of measurement matrices for a single-pixel-camera based on both theoretical and practical performance. In: *Emerging Imaging and Sensing Technologies for Security and Defence /V*. International Society for Optics and Photonics (2019).
40. Fienup JR. Phase retrieval algorithms: a comparison. *Applied optics* **21**, 2758–2769 (1982).
41. Jaganathan K, Eldar YC, Hassibi B. Phase retrieval: An overview of recent developments. *arXiv preprint arXiv:151007713*, (2015).
42. Cook JR, Bouchard RR, Emelianov SY. Tissue-mimicking phantoms for photoacoustic and ultrasonic imaging. *Biomedical optics express* **2**, 3193–3206 (2011).
43. Treeby BE, Cox BT. k-Wave: MATLAB toolbox for the simulation and reconstruction of photoacoustic wave fields. *Journal of biomedical optics* **15**, 021314 (2010).
44. LeCun Y, Bottou L, Bengio Y, Haffner P. Gradient-based learning applied to document recognition. *Proceedings of the IEEE* **86**, 2278–2324 (1998).
45. Jiao S, Gao Y, Feng J, Lei T, Yuan X. Does deep learning always outperform simple linear regression in optical imaging? *Optics Express* **28**, 3717–3731 (2020).
46. Jiao S, Feng J, Gao Y, Lei T, Xie Z, Yuan X. Optical machine learning with incoherent light and a single-pixel detector. *Optics letters* **44**, 5186–5189 (2019).

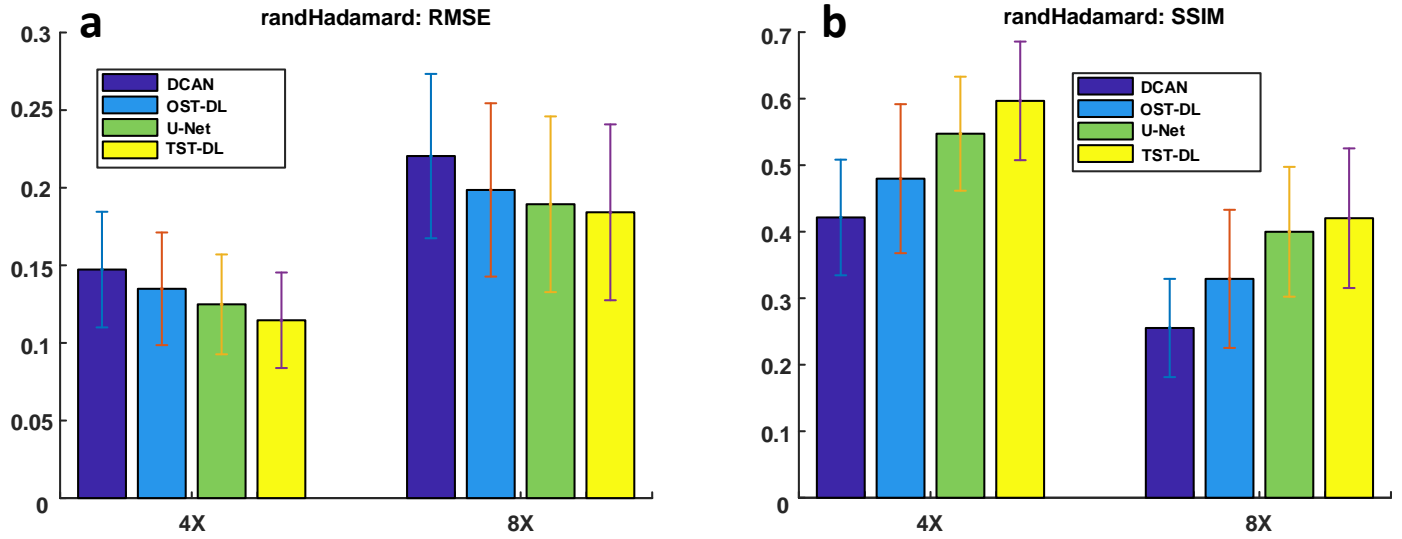
Supplementary information

Supplementary Table 1. Averaged RMSE and SSIM of the reconstructed images in the testing dataset at 4X and 8X compression ratios for different reconstruction approaches in single-pixel imaging with RD Hadamard patterns.

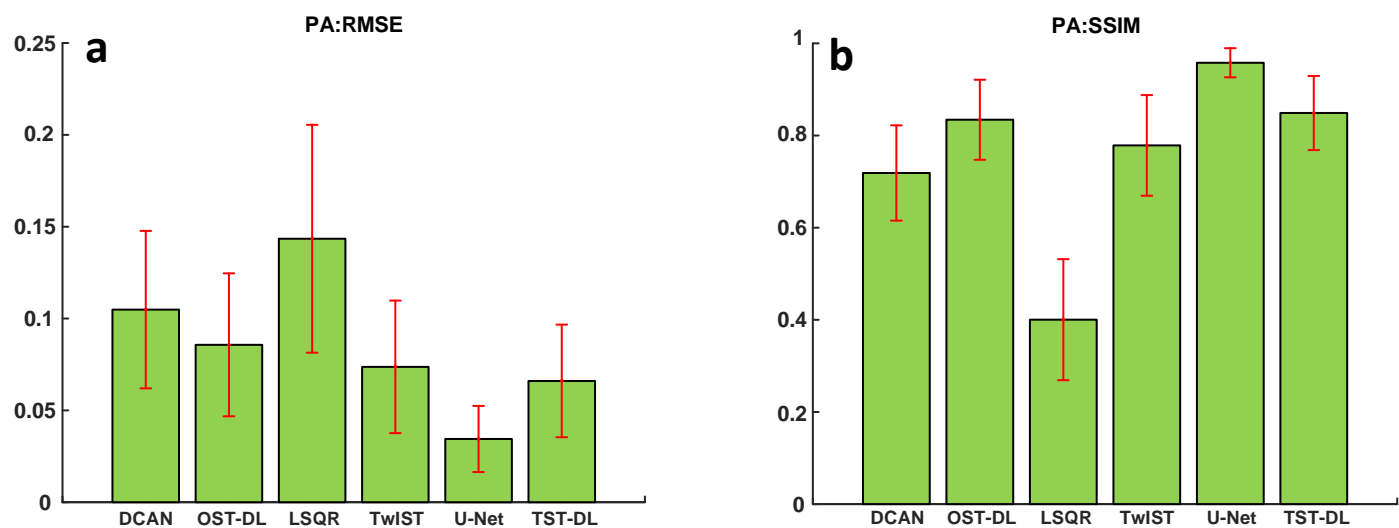
Compression Ratio		DCAN	OST-DL	LSQR	TwIST	U-Net	FCL-DL	TST-DL
4X	RMSE	0.079	0.059	0.060	0.051	0.050	0.051	0.051
	SSIM	0.798	0.803	0.830	0.865	0.865	0.816	0.833
8X	RMSE	0.086	0.079	0.072	0.061	0.059	0.063	0.063
	SSIM	0.711	0.700	0.706	0.780	0.787	0.727	0.762

Supplementary Table 2. Averaged RMSE and SSIM of the reconstructed images at 4X and 20X compression ratios for OST-DL, U-Net and TST-DL in experimental single-pixel imaging with random grayscale illumination patterns.

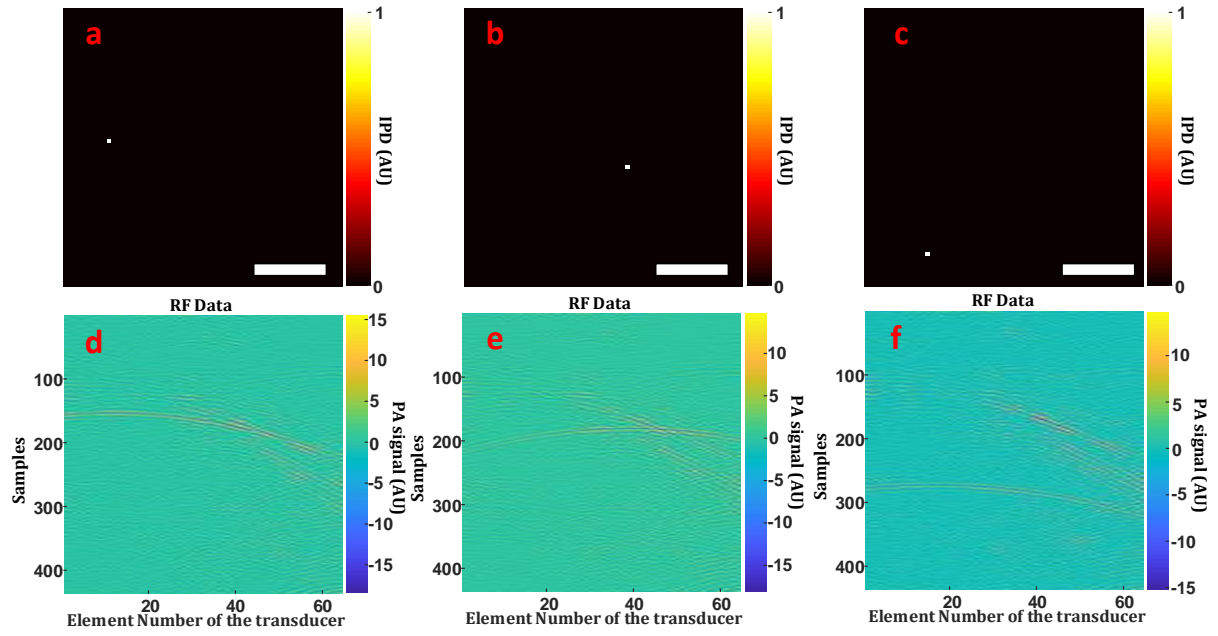
Compression Ratio		OST-DL	U-Net	TST-DL
4X	RMSE	0.241	0.104	0.143
	SSIM	0.597	0.873	0.797
20X	RMSE	0.259	0.170	0.164
	SSIM	0.568	0.735	0.748



Supplementary Fig. 1. Quantitative comparison in terms of RMSE and SSIM in single-pixel imaging with random Hadamard patterns. (a) RMSE for DCAN, OST-DL, U-Net and TST-DL with the random Hadamard patterns at 4X and 8X compression ratios. (b) SSIM for DCAN, OST-DL, U-Net and TST-DL with the random Hadamard patterns at 4X and 8X compression ratios.



Supplementary Fig. 2. Quantitative comparison in terms of RMSE and SSIM in PA imaging. (a) RMSE for DCAN, OST-DL, LSQR, TwIST, U-Net and TST-DL. (b) SSIM for DCAN, OST-DL, LSQR, TwIST, U-Net and TST-DL.



Supplementary Fig. 3. Representative images in the training dataset in experimental PA imaging. (a-c) IPD images as the output of the TST-DL network for training. (d-f) RF data of the impulse responses as the input of the TST-DL network for training after vectorization. The scale bar denotes 5mm.